

Direct Linearly-Polarised Electroluminescence from Perovskite Nanoplatelet Superlattices

Junzhi Ye ^{1,2}, Aobo Ren ^{3,4}, Linjie Dai ^{1*}, Tomi Baikie ¹, Renjun Guo ⁵, Debapriya Pal ⁶, Sebastian Gorgon ¹, Julian E. Heger ⁵, Junyang Huang ¹, Yuqi Sun ¹, Rakesh Arul ¹, Gianluca Grimaldi ⁶, Kaiwen Zhang ⁷, Javad Shamsi ¹, Yi-Teng Huang ¹, Hao Wang ⁸, Jiang Wu ⁴, A. Femius Koenderink ⁶, Laura Torrente Murciano ⁷, Matthias Schwartzkopf ⁹, Stephen V. Roth ^{9,10}, Peter Müller-Buschbaum ^{5, 11}, Jeremy J. Baumberg ¹, Samuel D. Stranks ^{1, 7}, Neil C. Greenham ¹, Lakshminarayana Polavarapu ¹², Wei Zhang ³, Akshay Rao ^{1*}, Robert L. Z. Hoye ^{2,13,*}

1. Cavendish Laboratory, University of Cambridge, JJ Thomson Ave, Cambridge CB3 0HE, United Kingdom
2. Inorganic Chemistry Laboratory, University of Oxford, South Parks Road, Oxford OX1 3QR, United Kingdom
3. Advanced Technology Institute, University of Surrey, Guildford, United Kingdom
4. Institute of Fundamental and Frontier Sciences, University of Electronic Science and Technology of China, Chengdu, China
5. Lehrstuhl für Funktionelle Materialien, Physik-Department, Technische Universität München, James-Franck-Str. 1, 85748 Garching, Germany
6. Centre for Nanophotonics, AMOLF, 1098 XG Amsterdam, The Netherlands
7. Department of Chemical Engineering and Biotechnology, University of Cambridge, Cambridge CB3 0AS, United Kingdom.
8. Division of Electrical Engineering, Department of Engineering, University of Cambridge, Cambridge, United Kingdom
9. Deutsches Elektronen-Synchrotron (DESY), Notkestrasse 85, D-22607 Hamburg, Germany
10. Department of Fibre and Polymer Technology, KTH Royal Institute of Technology, Teknikringen 56–58, Stockholm, 10044 Sweden
11. Heinz Maier-Leibnitz Zentrum (MLZ), Technische Universität München, Lichtenbergstr. 1, D-85748 Garching, Germany
12. CINBIO, Universidade de Vigo, Materials Chemistry and Physics Group, Department of Physical Chemistry, Campus Universitario As Lagoas, Marcosende, 36310 Vigo, Spain
13. Department of Materials, Imperial College London, Exhibition Road, London SW7 2AZ, United Kingdom

* Email: ld474@cam.ac.uk (L. D.), ar525@cam.ac.uk (A. R.), robert.hoye@chem.ox.ac.uk (R. L. Z. H.)

Abstract

Polarised light is critical for a wide range of applications, but is usually generated by filtering unpolarised light, which leads to significant energy losses and requires additional optics. Herein, the direct emission of linearly-polarised light is achieved from light-emitting diodes (LEDs) made of CsPbI₃ perovskite nanoplatelet superlattices. Through use of solvents with different vapour pressures, the self-assembly of perovskite nanoplatelets is achieved to enable fine control over the orientation (either face-up or edge-up) and therefore the transition dipole moment. As a result of the highly-uniform alignment of the nanoplatelets, as well as their strong quantum and dielectric confinement, large exciton fine-structure splitting is achieved at the film level, leading to pure-red LEDs exhibiting a high degree of linear polarisation of 74.4% without any photonic structures. This work unveils the possibilities of perovskite nanoplatelets as a highly promising source of linearly-polarised electroluminescence, opening up the development of next-generation 3D displays and optical communications from this highly versatile, solution-processable system.

Keywords: Colloidal perovskite nanoplatelets, self-assembly, polarised light emission, orientation control, stable pure-red LEDs, defect passivation, exciton fine-structure splitting

Linearly-polarised light is essential in numerous applications, including radiometric analysis, bio-imaging, counterfeit detection, liquid crystal displays, and emerging 3D display technologies¹⁻⁸. Conventionally, linear polarisation is obtained by passing unpolarised light through a linear polariser, which is typically constructed from highly-oriented long-chain molecules or wire grids with photonic structures, reducing the intensity by a factor of two or more^{1,8}. Organic molecules with aligned transition dipole moments (TDMs) can enable LEDs with linearly polarised electroluminescence (see Supplementary Table 1 for a comparison of reported materials), but the degree of polarisation (DOP) achieved until now have only been below 40%⁹⁻¹¹. Photonic structures, such as Ag nanogratings, are generally needed to generate higher DOPs (see Supplementary Table 1)¹². On the other hand, individual single particles of anisotropic inorganic nanostructures (e.g., cadmium selenide nanorods or indium phosphide nanowires) can achieve linearly polarised PL with DOP exceeding 70% (see Supplementary Table 1)^{1,2,13-21}. However, the DOP values significantly decrease when integrating single particles together to form nanoparticle films without using patterned photonic substrates because the nanoparticles would then have a random orientation, which limits the ability to translate the polarised emission from single particles to the device level^{1,18,22}. Therefore, approaches are needed to finely control the orientation of the anisotropic nanostructures in order to achieve high DOPs in films and devices.

Colloidal perovskite nanocrystals are a promising emerging class of light-emitting materials for display applications²³. Importantly, it has been shown that perovskite nanocrystals can self-assemble^{24,25}. Their bandgaps can be tuned over the entire visible to near-infrared wavelength

ranges by controlling the composition and dimensionality^{23,26,27}. Furthermore, perovskite nanocrystals benefit from defect tolerance in low-bandgap compositions, such as iodide-based perovskites²⁸, and can be passivated using a wide variety of approaches, enabling high photoluminescence quantum yields (PLQYs) reaching up to unity^{24,25,29-31}. Halide perovskites can also be fabricated as anisotropic nanostructures, such as nanoplatelets and nanowires, which have been reported to yield high DOPs in PL³²⁻³⁴, and are therefore promising for generating linearly polarised light. Becker *et al.* found that caesium lead halide nanocrystals have an exciton fine structure with distinct bright triplet states, and this could deliver strong linearly polarised emission^{34,35}. Seminal works on controlling the transition dipole moment (TDM) alignment in weakly-confined CsPbBr₃ nanoplatelets (9±2 nm thickness, >10 monolayers) have recently appeared^{36,37}. But as far as the authors are aware, there is no report on the orientation-controlled self-assembly of strongly-confined perovskite NPLs (*i.e.*, NPLs with thicknesses smaller than the exciton Bohr radius), and no demonstration of direct emission of high linearly-polarised EL from halide perovskite LEDs.

In this work, we overcome these pressing challenges to achieve linearly polarised EL directly from perovskite LEDs, which we demonstrate with colour-pure CsPbI₃ NPLs. To do this, we focus on addressing four critical factors. The first is in devising a synthesis route to achieve CsPbI₃ NPLs with a high degree of uniformity (necessary to achieve colour-pure emission), as well as strong quantum confinement (necessary to achieve exciton fine-structure splitting and polarised emission). The second is in self-assembling these CsPbI₃ NPLs with aligned TDMs. We investigate the use of solvents with different evaporation rates on the preferred orientation

of the NPLs, and the uniformity in their preferred orientation. The third factor is in ensuring that the materials have exciton-dominated radiative recombination, and minimising the influence of surface defects on non-radiative recombination. This requires effective defect passivation to achieve high photoluminescence quantum yields (PLQYs) more efficient LEDs. The final factor is to achieve a sufficiently large exciton fine-structure splitting to give high EL DOPs. This requires not only strong quantum confinement, but also dielectric confinement in a cubic lattice.

To address these four factors, we utilised structural (transmission electron microscopy, TEM; grazing-incidence wide-angle X-ray scattering, GIWAXS), optical (k -space Fourier microscopy) and first-principles analyses to understand the self-assembly properties and dipole alignment of the films. We measured the PL spectra at 5.2 K to compare the fine-structure splitting energy of the strongly-confined NPLs against a weakly-confined nanocube reference. We demonstrated pure-red CsPbI₃ LEDs with an EL DOP of 74.4%, which, to our knowledge, is the highest EL DOP for any organic or inorganic emitter reported thus far (Supplementary Table 1). The LEDs reported herein achieve an EQE of 2.7%, to our knowledge the highest for any strongly-confined perovskite emitter, in addition to being the first demonstration of pure-red EL from inorganic perovskite NPL LEDs.

Uniform, strongly-confined CsPbI₃ nanoplatelets with colour-pure luminescence

CsPbI₃ NPLs were synthesised by the spontaneous crystallisation method using a nonpolar toluene solvent for PbI₂ precursors and oleic acid for Cs-acetate precursors (see Methods)³⁸.

The PL spectra and TEM images of the synthesised NPIs are given in Fig. 1 and Supplementary Fig. 1. Previously-reported CsPbI₃ NPIs had a shoulder in the PL³⁸. To eliminate this and achieve colour-pure emission, we carefully investigated the effects of the precursors used, reaction temperature, and ratio in which the precursors were mixed, as shown in Supplementary Fig. 2a-c. We found that using caesium carbonate as a precursor led to a bimodal thickness distribution because carbonate reacts with the oleic acid ligands to form water that could damage NPIs by removing surface ligands and cause agglomeration. This was addressed by switching to acetate as the spectator anion, as well as lowering the reaction temperature using an ice bath in order to reduce the growth rate of the NPIs. In addition, by reducing the quantity of the caesium acetate precursor, we avoided NC formation (further details in Supplementary Note 1). The size distribution of the optimised NPIs was analysed by TEM, confirming that the NPIs have a length of 22±2 nm, width of 22±3 nm and a thickness of 2.6±0.5 nm (Supplementary Fig. 2d). The thickness of the NPIs was much smaller than the Bohr radius of CsPbI₃ (~12 nm)³⁹, and therefore a strong excitonic peak was observed in the absorption spectra (Fig. 1b-d). The centre of the PL was at approximately 600 nm (3 monolayer NPIs; see spectra in Fig. 1 b-d), which is blue-shifted compared with weakly-confined CsPbI₃ NCs (emitting at 700 nm wavelength).

Controlling the orientation of CsPbI₃ nanoplatelets through self-assembly

We developed a strategy for NPI orientation control based on their self-assembly at the solid-air interface upon the controlled evaporation of solvents with different vapour pressures⁴⁰. After centrifuging the crude solution at 22 769 RCF (*g*) (14 000 rpm) for 10 min, the precipitated

NPIs were dispersed in solvents with different boiling points (bp) and vapour pressures (p_v): hexane (bp = 69 °C, p_v = 20.49 kPa), cyclohexane (bp = 80.75 °C, p_v = 13.01 kPa), and heptane (bp = 98.42 °C, p_v = 6.08 kPa). The use of solvents with different bp and p_v changes the evaporation rate of the solvents during spin-coating. As a result, the NPIs can be kinetically trapped on the substrate to form films with different orientations without changing their dimensions, thus maintaining their absorption and PL profiles (Fig. 1b-d). For a slowly-evaporating solvent, such as heptane, the NPIs adopted a face-down orientation (Fig. 1b). By contrast, using a fast-evaporating solvent, such as hexane, resulted in an edge-up orientation (Fig. 1d). Additional TEM images with smaller magnification showing NPIs with different orientations can be found in Supplementary Fig. 1.

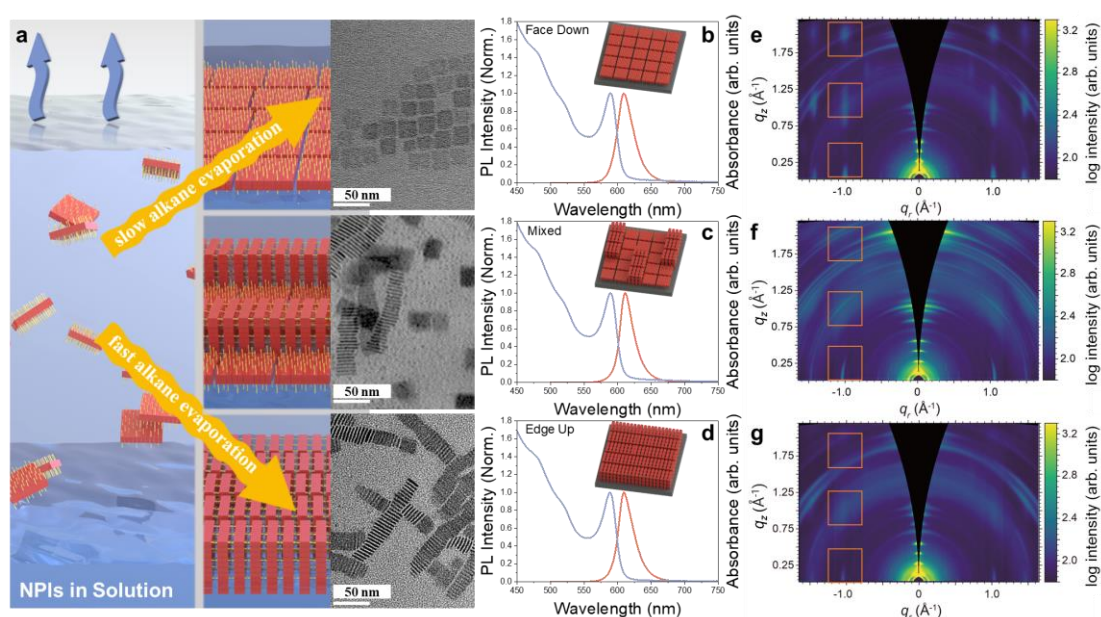


Fig. 1 | Orientation control of self-assembled CsPbI₃ nanoplatelets. **a**, Schematic illustrating how the orientation of the NPIs could be controlled by adjusting the solvent evaporation rate. The insets show TEM images of the face-down (top), mixed (middle) and edge-up (bottom) NPIs. **b-d**, Steady state PL and UV-Vis spectra of face-down, mixed, and edge-up NPI films, respectively. GIWAXS patterns of **e**, face-down, **f**, mixed and **g**, edge-up NPI films.

The change in NPI orientation was corroborated by GIWAXS measurements (Fig. 1 e-g). Films with face-down NPIs (Fig. 1e) showed strongly observable peaks associated with (100), (101)

and (102) planes (highlighted in the orange boxes from bottom to top, respectively), which became weaker and non-existent in the mixed (Fig. 1f) and edge-up (Fig. 1g) films, respectively⁴¹. In addition, the spread in the scattering of X-rays perpendicular to the diffraction rings in Fig. 1e confirms the layer-by-layer stacking of NPIs in the face-down orientation. Vertical stacking of the NPIs when they were face-down resulted in more repetitive planes than if they were edge-up, leading to stronger diffraction from these periodic planes; please refer to the intensity difference of the fringe inside the orange box for Fig. 1e and Fig. 1g⁴¹.

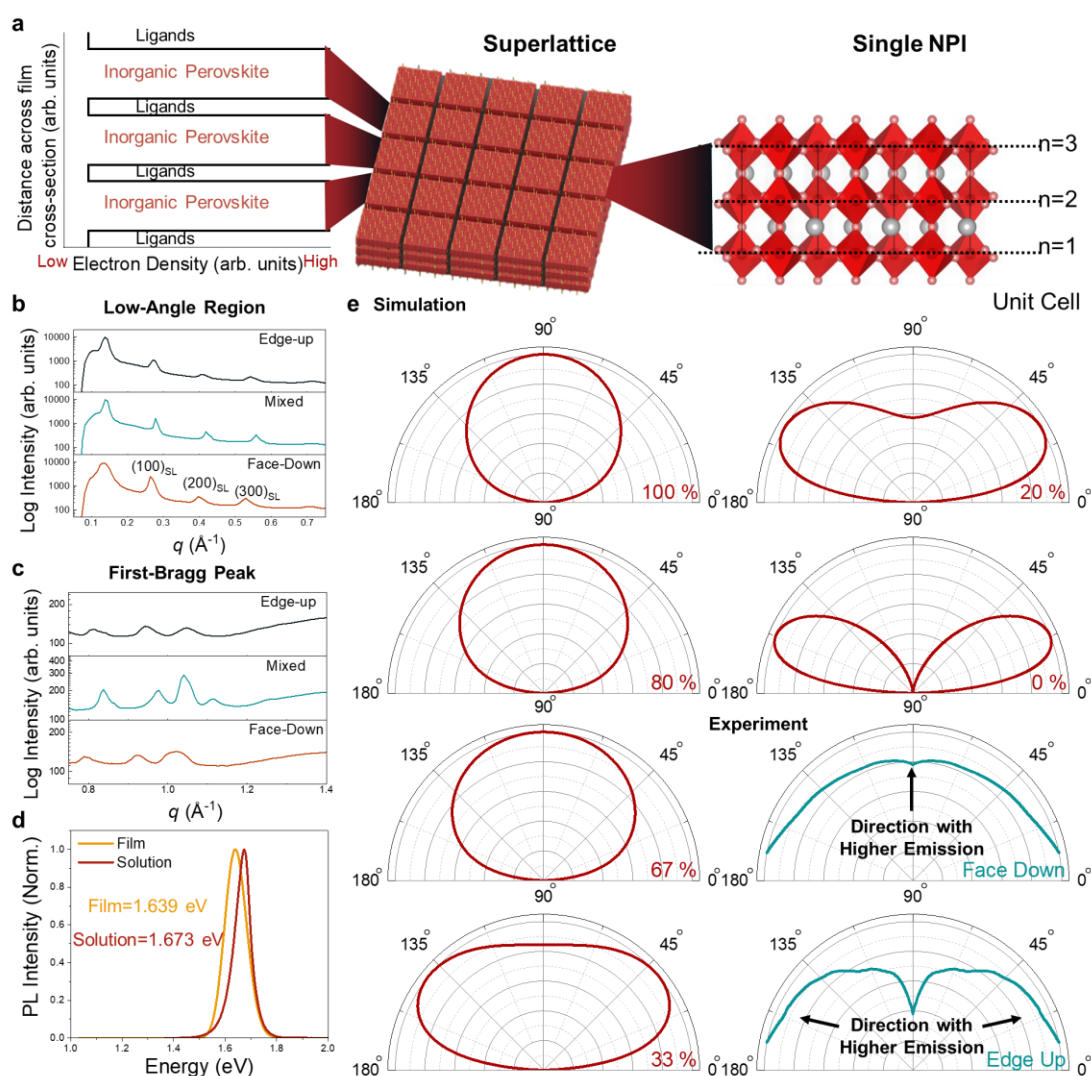


Fig. 2 | Structural and optical characterisation of self-assembled NPI films. a, Illustration of superlattices formed from the stacking of multiple NPIs, and how the electron density changes between inorganic perovskites and organic ligands. **b**, Line cut of the low angle region

in the GIWAXS measurements which demonstrates the formation of a superlattice. **c**, Line cut of the first Bragg peak region in the GIWAXS measurements. **d**, The PL of the NPIs in solution and films. The red shift in PL from solution to film could be caused by the self-assembled structures, as the NPIs are stacking together, the thickness or electronic coupling might be altered. **e**, Simulated (red) and experimental (blue) outcoupling from NPI films. Simulated light outcoupling of the NPIs films with different percentages of horizontal transition dipole moment (100% = all NPIs face-down, whereas 0% = all NPIs edge-up) to represent different degrees of preferred orientation of the NPIs, assuming the outcoupling contribution of the TDM in the confined direction is negligible. The simulated radiation patterns are integrated over the azimuth coordinate as a function of the polar angle (see Methods for details on the simulations). Experimental measurements of the angle-dependent PL obtained from *k*-space Fourier Microscopy are shown in blue. Details on data collection and analysis can be found in Supplementary Fig. 3. 0° is where the collection is parallel to the substrate, and 90° is where the collection is normal to the substrate.

The analysis of line cuts in the GIWAXS data reveals that the high degree of NPI orientation is related to the formation of superlattices during film formation. A schematic of a NPI superlattice is shown in Fig. 2a, depicting face-down NPIs stacked vertically and separated by organic ligands. The regular variation in electron density across the cross-section of the superlattice between the inorganic sub-lattice (high electron density) and organic ligands (low electron density), as illustrated in Fig. 2a, results in peaks in the low-angle scattering region from the GIWAXS scans (Fig. 2b) ^{36,41}. Another observation consistent with the formation of superlattices is the PL of the films having lower energy than those of CsPbI₃ NPIs in colloidal solution, as shown in Fig. 2d. This can be explained by two possible mechanisms. First, strong alignment of transition dipole moments in the strongly-confined NPIs (as occurs in superlattices) leads to lower-energy delocalised emissive states. Second, an increase in the dielectric constant of the surroundings around each NPI in superlattices (due to the presence of many high-dielectric constant NPIs) compared with isolated NPIs in solution, reduces the dielectric confinement^{42,43}. The red-shift in the PL of NPIs in films vs. colloidal solution was

approximately 34 meV, which matches with previous reports of PL red-shifts in superlattices of CsPbBr₃ and CsPbBr_{0.72}I_{0.28} nanocrystals (12-96 meV) compared with their isolated NCs.

42,43

Apart from structural evidence for self-assembly, optical analysis also provides strong evidence. Optical simulations of light emission from the films with different transition dipole alignments are shown in Fig. 2e. The labels inset in these red contour plots (100% to 0%) represent the percentage of TDMs that are horizontally aligned. These simulations showed that when the dipole was aligned out-of-plane (*i.e.*, 0% horizontal TDM, or perfectly edge-up NPIs), the vertical emission profile mainly came from the out-of-plane dipole (*i.e.*, along the thickness direction), leading to a lower PL intensity in the normal position compared to the horizontal direction. In contrast, when the NPIs were perfectly face-down (*i.e.*, 100% horizontal TDMs), the emission normal to the plane mainly came from the horizontal dipole, leading to stronger PL emission in the normal direction. Changing the NPI orientation from edge-up to face-down would therefore lead to an increase in the normal PL intensity due to an increase in the percentage of horizontal transition dipole moments contributing to this emission.^{15,36,37,44}

To validate the simulation results, angle-resolved PL was extracted from *k*-space Fourier microscopy measurements (Fig. 2e – blue plots; experimental details in Supplementary Fig. 3 and Supplementary Note 2). In the experimental results, 90° is where the collection was perpendicular to the substrates, and 0° is collection parallel to the substrates. The PL spectra at 90° and 11° can be found in Supplementary Fig. 3b and c. By integrating the PL spectra at each collection angle, we found that the edge-up NPI film had higher PL intensities at low collection

angles, which then decreased markedly as the collection angle increased. By contrast, the PL intensity for the face-down NPI films remained relatively constant over the range of collection angles (Fig. 2e and Supplementary Fig. 3c). These trends in angle-resolved PL agree with the simulation results. By sampling across five points in each film to eliminate random error, the same trends shown in Fig. 2e were observed. We note that the measured angle-resolved PL for the face-down NPIs had higher intensity at collection angles close to the substrate than expected from the simulations for 0% horizontal TDMs. This was because we assumed in the simulations that the TDMs in the confined direction (out-of-plane dipoles) to have negligible contribution to the emission profile. But when face-down NPIs stacked vertically to form superlattices, the emission from the out-of-plane dipoles would accumulate and lead to a non-negligible contribution towards the emission profile, thus accounting for more isotropic PL intensities observed over all collection angles. Moreover, it is difficult to accurately determine the percentage of in-plane TDMs using the current data, as the collection solid angle covered a few steradians, and the data was therefore averaged over several NPIs. Nevertheless, these data collectively suggest that the films have higher vertical outcoupling from face-down NPIs than edge-up NPIs.

The differences in light outcoupling with NPI orientation indicate that there was a substantial degree of dipole alignment in the films, which is beneficial for generating polarised emission¹⁵. For example, Achtstein and co-workers illustrated that single-particle NPIs have stronger directional emission with high linear polarisation than isotropic spherical quantum dots⁴⁴. Also, Gao and co-workers showed that aligning TDMs was critical to achieve polarised PL from

MAPbBr₃ polycrystalline films⁴⁵. Therefore, the demonstration of fine control over TDM alignment through the formation of self-assembled superlattices is highly promising for achieving polarised light emission.

Reducing non-radiative recombination through surface passivation

Before developing these self-assembled NPI films into LEDs, we first identified and reduced loss processes at NPI interfaces. We performed X-ray photoemission spectroscopy (XPS) measurements on the perovskite nanoplatelets, and found the surface to be terminated by Pb and I (Supplementary Fig. 4), with noticeable quantities of metallic Pb (Pb⁰). These Pb⁰ species, as well as possibly iodide vacancies, could limit the PLQY to 48±2% (Fig. 3a). We found that we could improve the PLQY to 65±1% by passivating the NPIs with PbI₂ coordinated with oleate and oleylamine ligands. The PbI₂ passivators could coordinate with Pb⁰ and fill I vacancies to reduce the density of recombination centres, especially at the surface. Full details are given in Supplementary Note 3.

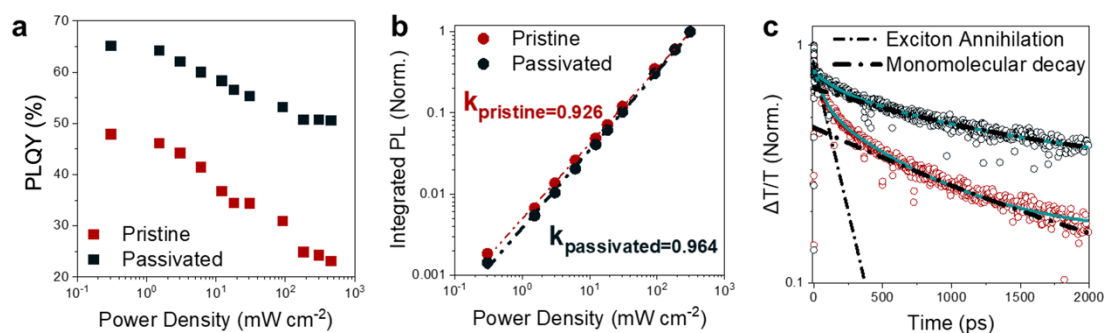


Fig. 3 | Photoluminescence quantum yield (PLQY) of pristine and passivated NPIs. a, Power-density dependent PLQY (405 nm CW laser excitation). **b,** Power-density (P) dependence of the integrated PL peak intensity. $I_{PL} \propto P^k$, where k is the exponent. When k is close to 1, radiative recombination proceeds in a monomolecular manner, consistent with the behaviour of excitons. **c,** Short timescale (0–2 ns time window) transient absorption spectroscopy measurements of the ground state bleach. Excitation was with a 400 nm wavelength pump laser, 301.5 $\mu\text{J cm}^{-2}$ pulse⁻¹ fluence, and 595 nm wavelength probe. All samples were in colloidal solution, measured in a cuvette with a 1 mm thick cavity.

As shown in Fig. 3a, the PLQY of the NPIs decreased with an increase in the excitation power density regardless of whether they were passivated. This trend contrasts to weakly-confined nanocrystal systems, where the PLQY usually increases with excitation power due to trap filling⁴⁶. The decrease in the PLQY of the NPIs with increasing power density was due to bimolecular exciton-exciton annihilation. Fig. 3b demonstrated a linear relationship between the PL intensity and excitation power density, indicating that we have a exciton dominated recombination system, which arises from the high exciton binding energies (243 meV; see later in Fig. 5f) due to strong dielectric and quantum confinement^{47,48}.

To understand in greater depth the effect of passivation on exciton kinetics, we measured time-resolved PL (TRPL) and transient absorption spectroscopy (TAS) of the NPI solutions. The governing equations and our method for determining the rate constants are discussed in Supplementary Note 3, with details in Supplementary Fig. 4–6. The fitting results are shown in Supplementary Table 2. This analysis shows that after PbI₂-ligand passivation, the monomolecular exciton radiative recombination rate (k_{rad}) decreased from 0.008 ns⁻¹ (pristine) to 0.004 ns⁻¹ (passivated). Meanwhile, the non-radiative monomolecular exciton trapping rate (k_{trap}) decreased from 0.009 ns⁻¹ (pristine) to 0.002 ns⁻¹ (passivated). Taken together, these results show that the recombination process in the NPIs became increasingly dominated by radiative processes after passivation (consistent with the PLQY measurements), and that the radiative lifetime of the excitons became longer. In addition, the non-radiative bimolecular exciton-exciton annihilation (EEA) rate decreased from 0.382 cm² s⁻¹ (pristine) to 0.282 cm² s⁻¹ (passivated). This can be seen from Fig. 3c for passivated and pristine NPI films. The dotted

line indicates the mono-exponential decay of the passivated films. When super-positioning the fitted bimolecular EEA and monomolecular decay of the passivated sample to the pristine sample in Fig. 3c, there is a clear mismatch of the fitting to the experimental data of the pristine sample, confirming that there were a trap-induced carrier losses at early timescales after excitation for the samples without passivation.

Linearly polarised LEDs with orientation-controlled CsPbI₃ nanoplatelets fulfilling Rec. 2020

Edge-up and face-down NPI films were fabricated into LEDs using the following structure: ITO//PEDOT:PSS/poly-TPD/NPIs/BCP/Ag (Fig. 4b inset). The EL spectra at different voltages (3.5-7 V) are shown in Fig. 4a. A red emission with CIE coordinates of (0.661, 0.338) was achieved, which is close to the Rec. 2020 standard for pure-red emission (Supplementary Fig. 7a). Unlike the mixed Br-I perovskite systems, the composition-purity of CsPbI₃ NPIs in the halide site enabled the devices to avoid halide segregation even at high applied biases (7 V)^{46,49}. It was only after increasing the applied bias from 3 V to well above the operational voltage with peak EQE that any changes in the EL spectrum became noticeable. At 7 V, the CIE coordinates marginally changed from (0.661, 0.338) at 3 V to (0.658, 0.341). This was due to the thermally-induced merging of NPIs due Joule heating from the high current density (approximately 1 mA cm⁻²) by this point. Through NPI orientation control, we increased the average EQE of the pristine devices (control) from 1.12% to 1.22% when changing the NPI orientation from edge-up to face-down by improving outcoupling (refer back to Fig. 2e). After adding the effects of surface passivation using PbI₂-ligand, the average EQE increased from 1.12% to 1.67% (edge-up NPIs), and from 1.22% to 2.38% (face-down NPIs) (Supplementary

Fig. 7b). The current injected was reduced after passivation, especially for the face-down NPI devices (Supplementary Fig. 7c). The champion NPI device (face-down NPIs with PbI_2 -ligand passivation) achieved 2.7% EQE at 4 V (1.25 mA cm^{-2}), with a maximum luminance of 408 cd m^{-2} obtained at 6V (49.95 mA cm^{-2}) (Fig. 4b, Supplementary Fig. 7d).

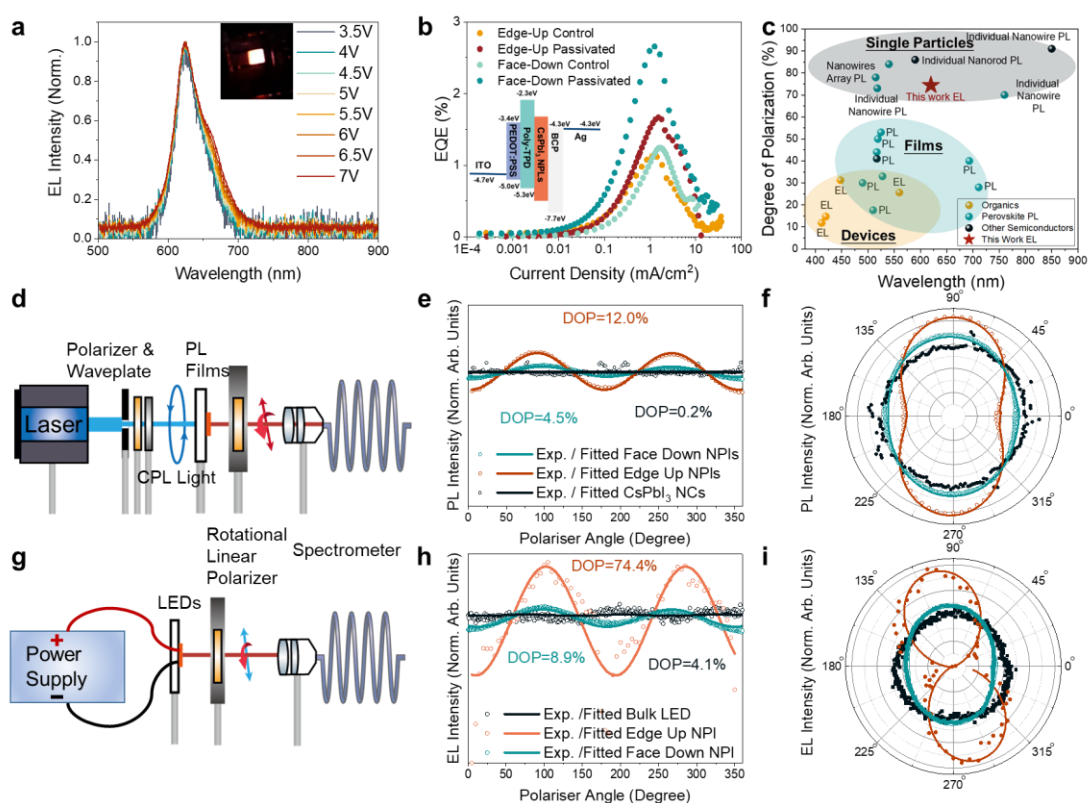


Fig. 4 | Linearly polarised emission from CsPbI_3 NPI films and devices. **a**, Electroluminescence (EL) spectra of optimised NPI LEDs from 3.5 V to 7 V. Inset shows the LED under operation (pixel area 0.16 cm^2). **b**, Current density against EQE for pristine and passivated edge-up and face-down NPI LEDs. Inset, the optimised LED device structure: ITO/PEDOT:PSS/poly-TPD/NPIs/BCP/Ag. **c**, Summary of degree of polarisation of different materials at single particle, film and device level. **d**, Schematic of producing and testing the polarised photoluminescence. **e**, Polarisation dependence of the PL for face-down, edge-up and bulk FAPbI_3 films at a fixed detection angle of 0° with respect to the substrate normal. **f**, Polar plots of the polarised PL. **g**, Schematic of producing and testing the polarised electroluminescence. **h**, Polarisation dependence of the EL for edge-up and bulk FAPbI_3 LEDs at a fixed detection angle of 0° with respect to the substrate normal. **i**, Polar plots of the polarised EL. The degree of polarisation, DOP, was calculated from: $\text{DOP} = (I_{\max} - I_{\min}) / (I_{\max} + I_{\min})$

The self-assembly of strongly-confined, and highly orientated NPIs led to strongly linearly

polarised EL from the LEDs, as shown in Fig. 4c-i. To measure the DOP, circularly polarised light (CPL) was generated by passing unpolarised light from the laser LEDs into a linear polariser and a waveplate. The emission of the sample was then passed through a linear polariser mounted onto an electrically driven rotation stage and coupled into a spectrometer. (Fig. 4d). The degree of polarisation of the EL was recorded in the same way (Fig. 4g). Both PL and EL showed clear polarised emission relative to more isotropic emitters, such as weakly-confined CsPbI₃ nanocube films and bulk FAPbI₃ thin film LEDs.

For the measurements of the DOP in PL (Fig. 4e), we found that the edge-up configuration (DOP=12%, PL) had a stronger degree of polarisation than the face-down NPLs (DOP=4.5%, PL), which is consistent with previous reports of self-assembled CdSe NPLs⁴⁰, as well as with theoretical predictions³⁵ (Fig. 4f). By contrast, the isotropic CsPbI₃ NC control sample had a low DOP of only 0.4% PL. To measure the DOP for EL, we accounted for changes in EL intensity over time under operation (Supplementary Fig. 7e and f) in order to extract only the changes in EL with the angle of the rotational linear polariser (Fig. 4g) over several cycles. For the edge-up LEDs, an EL DOP of 74.4% was achieved (Fig. 4h and i), which is the highest reported for any organic or inorganic LED without using photonic gratings (Supplementary Table 1 and Fig. 4c)^{18 50,51}. Notably, the DOP achieved in these film-based LEDs reached the single-particle level (Fig. 4c). In the next section, we discuss why the DOP for EL could exceed that for PL.

Strong degree of linear polarisation originating from large exciton fine-structure splitting

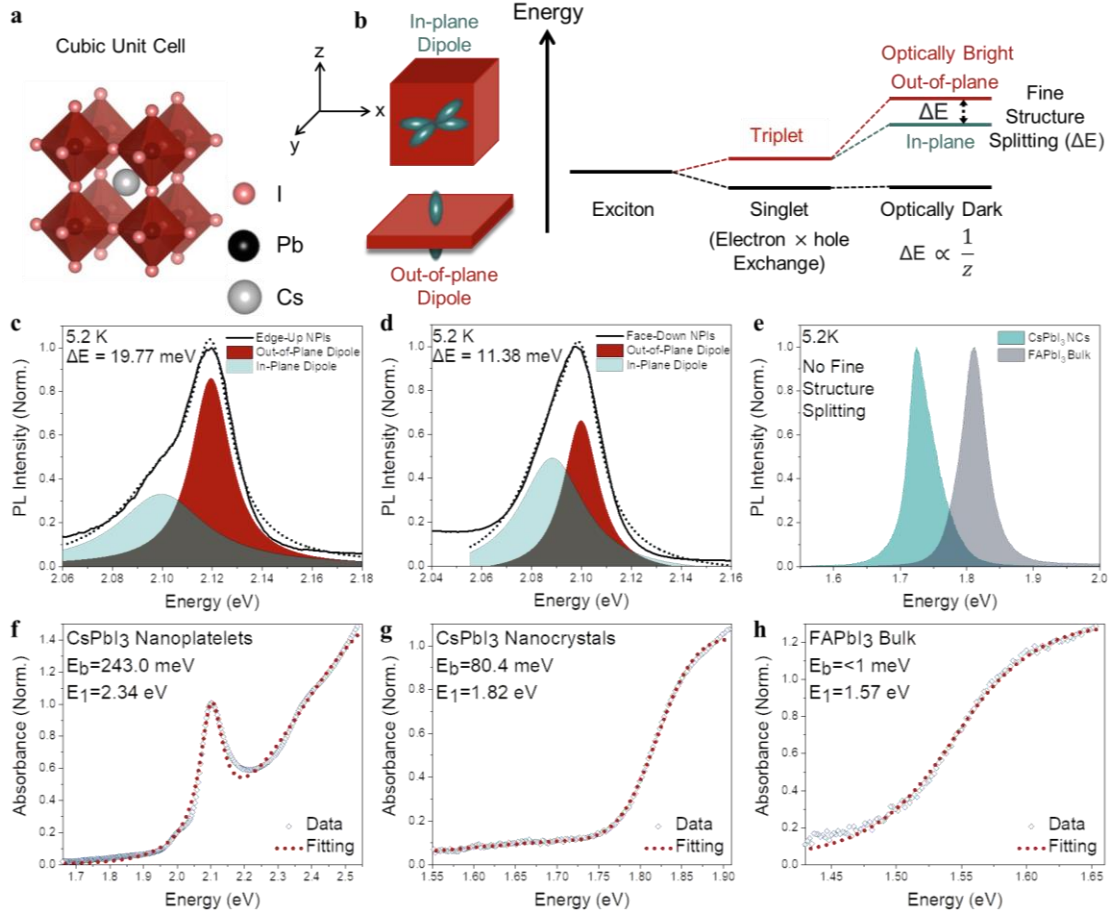


Fig. 5 | Origin of linearly polarised emission. **a**, Crystal structure of cubic (α -phase) CsPbI₃ ($Pm\bar{3}m$). **b**, Schematic diagram to illustrate the influence of quantum and dielectric confinement on exciton fine structure splitting (ΔE). The z -axis is across the thickness of the NPIs. Low temperature (5.2 K) PL spectra of **c**, edge-up and **d**, face-down NPI films. The fitted peaks represent the emission from the exciton fine structure. In these measurements, the detector was held perpendicular to the film. **e**, Low temperature (5.2 K) PL spectra of CsPbI₃ nanocubes and bulk FAPbI₃ thin films, from which no excitonic fine-structure splitting was observed. **f-g**, Elliot model fitting of the absorbance of CsPbI₃ NPIs, NCs and bulk FAPbI₃ to extract the exciton binding energy (E_b). E_1 is the first excited state. The fitting model used is based on Ref. 52 (fitting code from Ref. 53).

To understand the origin of the high DOP in the NPI films and devices, we measured the PL of the face-down and edge-up CsPbI₃ NPI films (Fig. 5a), and compared with weakly-confined CsPbI₃ NC films and FAPbI₃ bulk thin films at 5.2 K. Linearly polarised PL can arise from the fine-structure splitting (FSS) of band-edge excitons^{2,35}. In lead-halide perovskites, short- and

long-range electron–hole (e-h) exchange interactions result in a splitting of the band-edge excitonic states into an optically inactive singlet state with total angular momentum $j = 0$, and three optically active triplet states with $j = 1$ (Fig. 5b)⁵⁴. The triplet states can be split further into two or more energetic states in tetragonal or orthorhombic perovskites through crystal field effects⁵⁴, or in cubic perovskites through strong quantum and dielectric confinement^{35,55-57}. For example, Ghribi *et al.* showed through computational analyses that whilst non-confined cubic perovskites have degenerate optically-active triplets, the state with an out-of-plane dipole splits away from the two in-plane dipole states as the thickness of these nanocubes are reduced, and strongly quantum and dielectric confined nanoplatelets are realised³⁴ (see Fig. 5b for an illustration of this effect). Indeed, groups have reported the experimental observation of FSS from single particle CsPbBr₃ NPLs, *i.e.*, the PL spectra split into multiple peaks (1-3) at cryogenic temperature^{20,58}. However, the FSS reported was weak, and became especially difficult to observe at the film level when the NPLs or NCs were randomly distributed. In contrast to these previous experimental results, we were able to clearly observe PL splitting at 5.2 K at the film level (Fig. 5c and d), which may have been due to the uniform orientation of the NPLs and the alignment of their transition dipole moments through self-assembly. We extracted an FSS energy of 19.77 meV (edge-up) and 11.38 meV (face-down) by fitting the PL spectra we measured at 5.2 K. These values are significantly larger than the FSS energy of the reported isolated cuboidal NC (~ 1 meV)^{20,34}. Since our NPLs are strongly confined in the z -direction, the aspect ratio (thickness to length/width ratio) is very small (~ 0.13), and the FSS values we obtained for such small aspect ratio NPLs match well with predictions from previous theoretical analyses (~ 20 meV)³⁵.

Compared with the strongly-oriented NPI films we achieved here, no obvious FSS-induced PL splitting or polarised light emission were observed in weakly-confined NCs or bulk thin films (Fig. 5e). There are two possible reasons for this. Firstly, there is the lower exciton binding energy (E_b) in the NCs (80.4 meV) and bulk films (negligible) than in the NPIs (243 meV), as shown in Fig. 5f-h. All samples have the same cubic phase, so structural effects would have minimal impact compared to the effects of E_b . The smaller E_b in the NCs and bulk films would result in 1) radiative recombination not being solely due to excitons, and 2) a significantly reduced or negligible FSS. Secondly, there were no aligned TDMs in the NCs and bulk films, in contrast to the NPIs. Supplementary Fig. 9 shows the XRD patterns of drop-cast NPIs and NCs on glass substrates. Despite both of them having the same cubic phase, strong satellite peaks were only observed for the NPI films, which is consistent with superlattice formation⁵⁹. The lack of superstructures for NCs implies a more random orientation of TDMs in the films, thereby leading to no well-defined polarised emission.

We were able to fit two peaks to the low-temperature PL spectra of the NPIs (Fig. 5c,d). We attributed the higher energy PL peak to emission from the out-of-plane dipole (z -direction), and the lower-energy PL peak from the in-plane dipoles (x and y directions). The emission from each fine-structure state exhibits single polarisation, with the x - and y -direction polarisation being orthogonal to each other. Since we have similar sizes in the x - and y directions, these two states are essentially degenerate in α -CsPbI₃, and the overall emission would have negligible polarisation as they cancel each other out. Therefore, the linearly polarised emission from the NPIs would come from the higher energy state (z -direction dipole). From Fig. 5c,d, it can be seen that the edge-up films have stronger emission from these higher-energy states. This was

because the collection angle is normal to the film, and the emission in this direction has a strong contribution from the aligned out-of-plane dipole, which has higher energy level in the fine structure. This could explain why the edge-up film have a higher DOP than the face-down NPI films. However, the total DOP and PL splitting should be influenced by a combination of depolarisation within the FSS manifold due to energy transfer^{35,60}, the detection geometry relative to the crystal plane⁵⁸ and the local field effect⁶¹.

The EL DOP (74.4%) significantly exceeded the PL DOP (12.0%), and this could be explained by further increases in dipole alignment by the applied electric field during LED operation that leads to most of the injected carriers recombining at one particular energy level with minimal energy transfer to other triplet states. This observation matches well with previous studies on GaAs quantum dots, in which an increase in the DOP was also observed after increasing the applied electrical field⁶².

Conclusion

In conclusion, we have made the first demonstration of the direct generation of linearly-polarised electroluminescence from halide perovskites through use of strongly-confined CsPbI₃ nanoplatelets. These nanoplatelet LEDs also fulfil Rec. 2020 and have 2.7% EQE, the highest reported thus far for strongly-confined NPI LEDs (Supplementary Fig. 8)²¹. The orientation of the NPIs, and hence the percentage of in-plane/out-of-plane transition dipole moments, can be manipulated by the evaporation rate of the solvent the colloidal NPIs are dispersed in. Both structural (TEM, GIWAXS) and optical (angular-resolved PL) characterisation confirmed our

ability to control the orientation of NPI films through self-assembly. Detailed carrier dynamics measurements using time-resolved photoluminescence and transient absorption spectroscopy helped us to develop a passivation process for CsPbI₃ NPIs that reduced both monomolecular trap-assisted-recombination and bimolecular exciton-exciton annihilation. Importantly, we demonstrated a high degree of linear polarisation (74.4%) in the EL from pure-red LED devices, which is attributed to three key factors: 1) highly uniform alignment of the NPIs, 2) high PLQYs, such that the emission is strongly governed by the radiative recombination of band-edge excitons, and 3) large exciton fine structure splitting due to strong quantum and dielectric confinement, which was preserved at the film-level due to the formation of strongly-aligned NPI superlattices. This work opens up a new frontier in enabling applications for displays and optical communications with more efficient linearly polarised LEDs.

References

- 1 Wang, M., Yang, Z. & Zhang, C. Polarized Photoluminescence from Lead Halide Perovskites. *Adv. Opt. Mater.* **9**, 2002236, doi:<https://doi.org/10.1002/adom.202002236> (2021).
- 2 Ge, Y., Meng, L., Bai, Z. & Zhong, H. Linearly polarized photoluminescence from anisotropic perovskite nanostructures: emerging materials for display technology. *Journal of Information Display* **20**, 181-192, doi:10.1080/15980316.2019.1654550 (2019).
- 3 Geng, J. Three-dimensional display technologies. *Adv. Opt. Photon.* **5**, 456-535, doi:10.1364/AOP.5.000456 (2013).
- 4 Cunningham, P. D. *et al.* Assessment of Anisotropic Semiconductor Nanorod and Nanoplatelet Heterostructures with Polarized Emission for Liquid Crystal Display Technology. *ACS Nano* **10**, 5769-5781, doi:10.1021/acsnano.5b07949 (2016).
- 5 Wyatt, C. L. in *Radiometric Calibration: Theory and Methods* (ed Clair L. Wyatt) 151-162 (Academic Press, 1978).
- 6 Bloxham, W., Brinks, D., Kheifets, S. & Cohen, A. E. Linearly polarized excitation enhances signals from fluorescent voltage indicators. *Biophys. J.* **120**, 5333-5342, doi:<https://doi.org/10.1016/j.bpj.2021.10.028> (2021).

- 7 Pei, K. *et al.* Polarized Emission of Lanthanide Metal–Organic Framework (Ln-MOF) Crystals for High-Capacity Photonic Barcodes. *Adv. Opt. Mater.* **10**, 2102143, doi:<https://doi.org/10.1002/adom.202102143> (2022).
- 8 Srivastava, A. K. *et al.* Photoaligned Nanorod Enhancement Films with Polarized Emission for Liquid-Crystal-Display Applications. *Advanced Materials* **29**, 1701091, doi:<https://doi.org/10.1002/adma.201701091> (2017).
- 9 Geng, Y., Culligan, S. W., Trajkovska, A., Wallace, J. U. & Chen, S. H. Monodisperse Oligofluorenes Forming Glassy-Nematic Films for Polarized Blue Emission. *Chemistry of Materials* **15**, 542–549, doi:10.1021/cm0208859 (2003).
- 10 Culligan, S. W. *et al.* Strongly Polarized and Efficient Blue Organic Light-Emitting Diodes Using Monodisperse Glassy Nematic Oligo(fluorene)s. *Advanced Materials* **15**, 1176–1180, doi:<https://doi.org/10.1002/adma.200304972> (2003).
- 11 Chen, A. C. A. *et al.* Organic Polarized Light-Emitting Diodes via Förster Energy Transfer Using Monodisperse Conjugated Oligomers. *Advanced Materials* **16**, 783–788, doi:<https://doi.org/10.1002/adma.200306265> (2004).
- 12 Ming Yi, L., Yi Jiun, C., Hoang Yan, L. & Si-Chen, L. in *2012 12th IEEE International Conference on Nanotechnology (IEEE-NANO)*. 1–4.
- 13 Hu, J. *et al.* Linearly Polarized Emission from Colloidal Semiconductor Quantum Rods. *Science* **292**, 2060–2063, doi:10.1126/science.1060810 (2001).
- 14 Wang, J., Gudiksen, M. S., Duan, X., Cui, Y. & Lieber, C. M. Highly Polarized Photoluminescence and Photodetection from Single Indium Phosphide Nanowires. *Science* **293**, 1455–1457, doi:10.1126/science.1062340 (2001).
- 15 Jurow, M. J. *et al.* Manipulating the Transition Dipole Moment of CsPbBr₃ Perovskite Nanocrystals for Superior Optical Properties. *Nano Lett.* **19**, 2489–2496, doi:10.1021/acs.nanolett.9b00122 (2019).
- 16 Liu, J. *et al.* Polarized emission from single perovskite FAPbBr₃ nanocrystals. *Journal of Luminescence* **221**, 117032, doi:<https://doi.org/10.1016/j.jlumin.2020.117032> (2020).
- 17 Wang, J. *et al.* Strong Polarized Photoluminescence CsPbBr₃ Nanowire Composite Films for UV Spectral Conversion Polarization Photodetector Enhancement. *ACS Appl. Mater. Interfaces* **13**, 36147–36156, doi:10.1021/acsami.1c07681 (2021).
- 18 Lin, C.-H. *et al.* Giant Optical Anisotropy of Perovskite Nanowire Array Films. *Advanced Functional Materials* **30**, 1909275, doi:<https://doi.org/10.1002/adfm.201909275> (2020).
- 19 Yang, D. *et al.* Facet-induced coordination competition for highly ordered CsPbBr₃ nanoplatelets with strong polarized emission. *Nano Research* **15**, 502–509, doi:10.1007/s12274-021-3509-6 (2022).
- 20 Huo, C. *et al.* Optical Spectroscopy of Single Colloidal CsPbBr₃ Perovskite Nanoplatelets. *Nano Letters* **20**, 3673–3680, doi:10.1021/acs.nanolett.0c00611 (2020).
- 21 Otero-Martínez, C. *et al.* Colloidal Metal-Halide Perovskite Nanoplatelets: Thickness-Controlled Synthesis, Properties, and Application in Light-Emitting Diodes. *Advanced Materials* **34**, 2107105, doi:<https://doi.org/10.1002/adma.202107105> (2022).
- 22 Wei, Y. *et al.* CsPbBr₃ nanowire polarized light-emitting diodes through mechanical rubbing. *Chemical Communications* **56**, 5413–5416, doi:10.1039/C9CC10033D (2020).
- 23 Dey, A. *et al.* State of the Art and Prospects for Halide Perovskite Nanocrystals. *ACS Nano* **15**, 10775–10981, doi:10.1021/acsnano.0c08903 (2021).

- 24 Jana, A. *et al.* Self-assembly of perovskite nanocrystals. *Prog. Mater. Sci.* **129**, 100975, doi:<https://doi.org/10.1016/j.pmatsci.2022.100975> (2022).
- 25 Liu, J., Zheng, X., Mohammed, O. F. & Bakr, O. M. Self-Assembly and Regrowth of Metal Halide Perovskite Nanocrystals for Optoelectronic Applications. *Acc. Chem. Res.* **55**, 262-274, doi:10.1021/acs.accounts.1c00651 (2022).
- 26 Byranvand, M. M. *et al.* Recent Progress in Mixed A-Site Cation Halide Perovskite Thin-Films and Nanocrystals for Solar Cells and Light-Emitting Diodes. *Adv. Opt. Mater.* **10**, 2200423, doi:<https://doi.org/10.1002/adom.202200423> (2022).
- 27 Hoye, R. L. Z. *et al.* The Role of Dimensionality on the Optoelectronic Properties of Oxide and Halide Perovskites, and their Halide Derivatives. *Adv. Energy Mater.* **12**, 2100499, doi:<https://doi.org/10.1002/aenm.202100499> (2022).
- 28 Nenon, D. P. *et al.* Design Principles for Trap-Free CsPbX₃ Nanocrystals: Enumerating and Eliminating Surface Halide Vacancies with Softer Lewis Bases. *Journal of the American Chemical Society* **140**, 17760-17772, doi:10.1021/jacs.8b11035 (2018).
- 29 Bi, C. *et al.* Self-Assembled Perovskite Nanowire Clusters for High Luminance Red Light-Emitting Diodes. *Advanced Functional Materials* **30**, 2005990, doi:<https://doi.org/10.1002/adfm.202005990> (2020).
- 30 Tong, Y. *et al.* From Precursor Powders to CsPbX₃ Perovskite Nanowires: One-Pot Synthesis, Growth Mechanism, and Oriented Self-Assembly. *Angewandte Chemie International Edition* **56**, 13887-13892, doi:<https://doi.org/10.1002/anie.201707224> (2017).
- 31 Wu, Y. *et al.* In Situ Passivation of PbBr₆⁴⁻ Octahedra toward Blue Luminescent CsPbBr₃ Nanoplatelets with Near 100% Absolute Quantum Yield. *ACS Energy Lett.* **3**, 2030-2037, doi:10.1021/acsenerylett.8b01025 (2018).
- 32 Täuber, D., Dobrovolsky, A., Camacho, R. & Scheblykin, I. G. Exploring the Electronic Band Structure of Organometal Halide Perovskite via Photoluminescence Anisotropy of Individual Nanocrystals. *Nano Letters* **16**, 5087-5094, doi:10.1021/acs.nanolett.6b02012 (2016).
- 33 Ghoshal, D. *et al.* Catalyst-Free and Morphology-Controlled Growth of 2D Perovskite Nanowires for Polarized Light Detection. *Adv. Opt. Mater.* **7**, 1900039, doi:<https://doi.org/10.1002/adom.201900039> (2019).
- 34 Becker, M. A. *et al.* Bright triplet excitons in caesium lead halide perovskites. *Nature* **553**, 189-193, doi:10.1038/nature25147 (2018).
- 35 Ghribi, A. *et al.* Dielectric Confinement and Exciton Fine Structure in Lead Halide Perovskite Nanoplatelets. *Nanomaterials* **11** (2021).
- 36 Kumar, S. *et al.* Anisotropic nanocrystal superlattices overcoming intrinsic light outcoupling efficiency limit in perovskite quantum dot light-emitting diodes. *Nat. Commun.* **13**, 2106, doi:10.1038/s41467-022-29812-5 (2022).
- 37 Cui, J. *et al.* Efficient light-emitting diodes based on oriented perovskite nanoplatelets. *Science Advances* **7**, eabg8458, doi:10.1126/sciadv.abg8458 (2020).
- 38 Huang, H. *et al.* Spontaneous Crystallization of Perovskite Nanocrystals in Nonpolar Organic Solvents: A Versatile Approach for their Shape-Controlled Synthesis. *Angewandte Chemie International Edition* **58**, 16558-16562, doi:<https://doi.org/10.1002/anie.201906862> (2019).

- 39 Protesescu, L. *et al.* Nanocrystals of Cesium Lead Halide Perovskites (CsPbX₃, X = Cl, Br, and I): Novel Optoelectronic Materials Showing Bright Emission with Wide Color Gamut. *Nano Lett.* **15**, 3692-3696, doi:10.1021/nl5048779 (2015).
- 40 Momper, R. *et al.* Kinetic Control over Self-Assembly of Semiconductor Nanoplatelets. *Nano Letters* **20**, 4102-4110, doi:10.1021/acs.nanolett.9b05270 (2020).
- 41 Toso, S. *et al.* Multilayer Diffraction Reveals That Colloidal Superlattices Approach the Structural Perfection of Single Crystals. *ACS Nano* **15**, 6243-6256, doi:10.1021/acsnano.0c08929 (2021).
- 42 Baranov, D., Toso, S., Imran, M. & Manna, L. Investigation into the Photoluminescence Red Shift in Cesium Lead Bromide Nanocrystal Superlattices. *The Journal of Physical Chemistry Letters* **10**, 655-660, doi:10.1021/acs.jpcllett.9b00178 (2019).
- 43 Lapkin, D. *et al.* Spatially resolved fluorescence of caesium lead halide perovskite supercrystals reveals quasi-atomic behavior of nanocrystals. *Nat. Commun.* **13**, 892, doi:10.1038/s41467-022-28486-3 (2022).
- 44 Scott, R. *et al.* Directed emission of CdSe nanoplatelets originating from strongly anisotropic 2D electronic structure. *Nat. Nanotech.* **12**, 1155-1160, doi:10.1038/nnano.2017.177 (2017).
- 45 Qin, J. *et al.* Aligning Transition Dipole Moment toward Light Amplification and Polarized Emission in Hybrid Perovskites. *Adv. Opt. Mater.* **9**, 2100984, doi:<https://doi.org/10.1002/adom.202100984> (2021).
- 46 Ye, J. *et al.* Elucidating the Role of Antisolvents on the Surface Chemistry and Optoelectronic Properties of CsPbBr_{3-x} Perovskite Nanocrystals. *Journal of the American Chemical Society* **144**, 12102-12115, doi:10.1021/jacs.2c02631 (2022).
- 47 Liu, Q. *et al.* Exciton Relaxation Dynamics in Photo-Excited CsPbI₃ Perovskite Nanocrystals. *Scientific Reports* **6**, 29442, doi:10.1038/srep29442 (2016).
- 48 Protesescu, L. *et al.* Nanocrystals of Cesium Lead Halide Perovskites (CsPbX₃, X = Cl, Br, and I): Novel Optoelectronic Materials Showing Bright Emission with Wide Color Gamut. *Nano Letters* **15**, 3692-3696, doi:10.1021/nl5048779 (2015).
- 49 Hassan, Y. *et al.* Ligand-engineered bandgap stability in mixed-halide perovskite LEDs. *Nature* **591**, 72-77, doi:10.1038/s41586-021-03217-8 (2021).
- 50 Güner, T. *et al.* Polarized emission from CsPbBr₃ nanowire embedded-electrospun PU fibers. *Nanotechnology* **29**, 135202, doi:10.1088/1361-6528/aaaaf (2018).
- 51 Wang, D. *et al.* Polarized emission from CsPbX₃ perovskite quantum dots. *Nanoscale* **8**, 11565-11570, doi:10.1039/C6NR01915C (2016).
- 52 Kaiser, M. *et al.* How free exciton-exciton annihilation lets bound exciton emission dominate the photoluminescence of 2D-perovskites under high-fluence pulsed excitation at cryogenic temperatures. *J. Appl. Phys.* **129**, 123101, doi:10.1063/5.0037800 (2021).
- 53 Hoye, R. L. Z. *et al.* Identifying and Reducing Interfacial Losses to Enhance Color-Pure Electroluminescence in Blue-Emitting Perovskite Nanoplatelet Light-Emitting Diodes. *ACS Energy Lett.* **4**, 1181-1188, doi:10.1021/acsenerylett.9b00571 (2019).
- 54 Sercel, P. C. *et al.* Exciton Fine Structure in Perovskite Nanocrystals. *Nano Letters* **19**, 4068-4077, doi:10.1021/acs.nanolett.9b01467 (2019).
- 55 Han, Y. *et al.* Lattice distortion inducing exciton splitting and coherent quantum beating

- in CsPbI₃ perovskite quantum dots. *Nat. Mater.*, doi:10.1038/s41563-022-01349-4 (2022).
- 56 Takagahara, T. Effects of dielectric confinement and electron-hole exchange interaction on excitonic states in semiconductor quantum dots. *Physical Review B* **47**, 4569-4584, doi:10.1103/PhysRevB.47.4569 (1993).
- 57 Rajadell, F., Climente, J. I. & Planelles, J. Excitons in core-only, core-shell and core-crown CdSe nanoplatelets: Interplay between in-plane electron-hole correlation, spatial confinement, and dielectric confinement. *Physical Review B* **96**, 035307, doi:10.1103/PhysRevB.96.035307 (2017).
- 58 Schmitz, A. *et al.* Optical Probing of Crystal Lattice Configurations in Single CsPbBr₃ Nanoplatelets. *Nano Letters* **21**, 9085-9092, doi:10.1021/acs.nanolett.1c02775 (2021).
- 59 Toso, S., Baranov, D., Filippi, U., Giannini, C. & Manna, L. Collective Diffraction Effects in Perovskite Nanocrystal Superlattices. *Acc. Chem. Res.* **56**, 66-76, doi:10.1021/acs.accounts.2c00613 (2023).
- 60 Gramlich, M. *et al.* Dark and Bright Excitons in Halide Perovskite Nanoplatelets. *Adv. Sci.* **9**, 2103013, doi:<https://doi.org/10.1002/adv.202103013> (2022).
- 61 Rodina, A. V. & Efros, A. L. Effect of dielectric confinement on optical properties of colloidal nanostructures. *Journal of Experimental and Theoretical Physics* **122**, 554-566, doi:10.1134/S1063776116030183 (2016).
- 62 Ghali, M., Ohtani, K., Ohno, Y. & Ohno, H. Generation and control of polarization-entangled photons from GaAs island quantum dots by an electric field. *Nat. Commun.* **3**, 661, doi:10.1038/ncomms1657 (2012).
- 63 Buffet, A. *et al.* P03, the microfocus and nanofocus X-ray scattering (MiNaXS) beamline of the PETRA III storage ring: the microfocus endstation. *Journal of Synchrotron Radiation* **19**, 647-653, doi:10.1107/s0909049512016895 (2012).
- 64 Reus, M. A. *et al.* Time-Resolved Orientation and Phase Analysis of Lead Halide Perovskite Film Annealing Probed by In Situ GIWAXS. *Adv. Opt. Mater.* **10**, 2102722, doi:<https://doi.org/10.1002/adom.202102722> (2022).

Acknowledgements

J.Y. and R.L.Z.H. acknowledge support from a UK Research and Innovation (UKRI) Frontier Grant (no. EP/X029900/1), awarded via the European Research Council Starting Grant 2021 scheme. J.Y. also gives thanks to Cambridge Philosophical Society for the Research Studentship Grant and Churchill College for various travel and research grant. R.L.Z.H. thanks the Royal Academy of Engineering through the Research Fellowships scheme (no. RF\201718\1701), as well as the Centre of Advanced Materials for Integrated Energy Systems (CAM-IES; EPSRC grant no. EP/T012218/1). T.K.B. gives thanks to the Centre for Doctoral Training in New and Sustainable Photovoltaics (EP/L01551X/2) and the NanoDTC (EP/L015978/1) for financial support. L.D. thanks the Cambridge Trusts and the China Scholarship Council for funding. M.A.R. and P.M.-B. acknowledge funding from the Deutsche Forschungsgemeinschaft (DFG, German Research Foundation) within Germany's Excellence Strategy, EXC 2089/1-390,776,260 (e-conversion) and by TUM.solar in the context of the Bavarian Collaborative

Research Project Solar Technologies Go Hybrid (SolTech). R.A. acknowledges support from the Rutherford Foundation of the Royal Society Te Apārangi of New Zealand, the Winton Programme for the Physics of Sustainability, and Trinity College Cambridge. J.J.B. acknowledges support of ERC grant PICOFORCE (883703). K. Z. would like to acknowledge the EPSRC Centre for Doctoral Training in Graphene Technology (EP/L016087/1) for studentship. K.Z. and L.T.M would like to acknowledge EP/ P030467/1 equipment grant for the generation of microscopic data. The authors would like to thank Dr. Mark Isaacs for the collection of the X-ray photoelectron (XPS) data at the EPSRC National Facility for XPS (“HarwellXPS”), operated by Cardiff University and UCL, under Contract No. PR16195. This publication is part of the project NanoLEDs with project number 17100 of the research programme High Tech Systems and Materials which is (partly) financed by the Dutch Research Council (NWO). S.D.S. acknowledges the Royal Society and Tata Group (grant no. UF150033). The work has received funding from the European Research Council under the European Union’s Horizon 2020 research and innovation programme (HYPERION, grant agreement no. 756962; PEROVSCI, 957513). The authors acknowledge the EPSRC (EP/R023980/1, EP/S030638/1, EP/V061747/1) for funding. L.P. acknowledges support from the Spanish Ministerio de Ciencia e Innovación through Ramón y Cajal grant (RYC2018-026103-I) and the Spanish State Research Agency (Grant PID2020-117371RA-I00) and a grant from the Xunta de Galicia (ED431F2021/05).

Author contributions

J.Y. and R.L.Z.H. conceived of the project. L.D. contributed to part of the project design under the supervision of N.C.G and S.D.S. J.Y. J.S. and L.P. synthesised the materials and films. J.Y. and Y.H. performed the transient absorption spectroscopy measurement. J.Y., A.R., J.W. and W.Z. optimised devices. T.B. performed the polarisation measurements. R.G., J.E.H, M.S. S.V.R, and P.M.B. performed the GIWAXS measurement and analysis. D.P., G.G. and A.F. K. constructed the optical simulation model. J.Y. and S.G. performed the low temperature PL measurement. J.H., R. A and J.J B performed and analysed the *k*-space Fourier microscopy measurement. Y.S. supplied the FAPbI₃ LEDs. K.Z. and L.T.M performed the TEM measurements. A.R. and R.L.Z.H. supervised the work. All authors contributed to writing and editing the manuscript.

Conflicts of Interest

Authors declare no competing interests.